



Bacterioferritin of *Magnetospirillum gryphiswaldense* Is a Heterotetraeicosameric Complex Composed of Functionally Distinct Subunits but Is Not Involved in Magnetite Biomineralization

René Uebe,^a Frederik Ahrens,^a Jörg Stang,^a Katharina Jäger,^b Lars H. Böttger,^{b*} Christian Schmidt,^b Berthold F. Matzanke,^b Dirk Schüler^a

^aDepartment of Biology, Chemistry and Geosciences, Universität Bayreuth, Bayreuth, Germany

^bIsotopes Laboratory, Section Sciences, Universität zu Lübeck, Lübeck, Germany

ABSTRACT The biomineralization pathway of magnetite in magnetotactic bacteria is still poorly understood and a matter of intense debates. In particular, the existence, nature, and location of possible mineral precursors of magnetite are not clear. One possible precursor has been suggested to be ferritin-bound ferrihydrite. To clarify its role for magnetite biomineralization, we analyzed and characterized ferritin-like proteins from the magnetotactic alphaproteobacterium *Magnetospirillum gryphiswaldense* MSR-1, employing genetic, biochemical, and spectroscopic techniques. Transmission Mössbauer spectroscopy of the wild type (WT) and a bacterioferritin (*bfr*) deletion strain uncovered that the presence of ferrihydrite in cells is coupled to the presence of Bfr. However, *bfr* and *dps* deletion mutants, encoding another ferritin-like protein, or even mutants with their codeletion had no impact on magnetite formation in MSR-1. Thus, ferritin-like proteins are not involved in magnetite biomineralization and Bfr-bound ferrihydrite is not a precursor of magnetite biosynthesis. Using transmission electron microscopy and bacterial two-hybrid and electrophoretic methods, we also show that MSR-1 Bfr is an atypical representative of the Bfr subfamily, as it forms tetraeicosameric complexes from two distinct subunits. Furthermore, our analyses revealed that these subunits are functionally divergent, with Bfr1 harboring a ferroxidase activity while only Bfr2 contributes to heme binding. Because of this functional differentiation and the poor formation of homooligomeric Bfr1 complexes, only heterooligomeric Bfr protects cells from oxidative stress *in vivo*. In summary, our results not only provide novel insights into the biomineralization of magnetite but also reveal the unique properties of so-far-uncharacterized heterooligomeric bacterioferritins.

IMPORTANCE Magnetotactic bacteria like *Magnetospirillum gryphiswaldense* are able to orient along magnetic field lines due to the intracellular formation of magnetite nanoparticles. Biomineralization of magnetite has been suggested to require a yet-unknown ferritin-like ferrihydrite component. Here, we report the identification of a bacterioferritin as the source of ferrihydrite in *M. gryphiswaldense* and show that, contrary to previous reports, bacterioferritin is not involved in magnetite biomineralization but required for oxidative stress resistance. Additionally, we show that bacterioferritin of *M. gryphiswaldense* is an unusual member of the bacterioferritin subfamily as it is composed of two functionally distinct subunits. Thus, our findings extend our understanding of the bacterioferritin subfamily and also solve a long-standing question about the magnetite biomineralization pathway.

KEYWORDS bacterioferritin, biomineralization, ferritin, magnetite, oxidative stress, prokaryotic organelle

Citation Uebe R, Ahrens F, Stang J, Jäger K, Böttger LH, Schmidt C, Matzanke BF, Schüler D. 2019. Bacterioferritin of *Magnetospirillum gryphiswaldense* is a heterotetraeicosameric complex composed of functionally distinct subunits but is not involved in magnetite biomineralization. *mBio* 10:e02795-18. <https://doi.org/10.1128/mBio.02795-18>.

Editor Arash Komeili, University of California, Berkeley

Copyright © 2019 Uebe et al. This is an open-access article distributed under the terms of the [Creative Commons Attribution 4.0 International license](https://creativecommons.org/licenses/by/4.0/).

Address correspondence to René Uebe, rene.uebe@uni-bayreuth.de, or Berthold F. Matzanke, matzanke@isolab.uni-luebeck.de.

* Present address: Lars H. Böttger, Stanford University, Stanford, California, USA.

Received 12 December 2018

Accepted 12 April 2019

Published 21 May 2019

Iron is essential for almost all organisms. Because of its versatile biochemical properties, it serves as a cofactor in a multitude of biochemical reactions, including respiration, photosynthesis, or DNA synthesis (1). However, excess iron can be toxic due to its ability to increase the formation of reactive oxygen species via the Fenton reaction (2). To avoid iron-mediated toxicity, bacteria use regulatory sensor proteins (e.g., ferric uptake regulator [Fur]) to determine intracellular iron concentrations and transcriptionally control genes involved in the import, efflux, and metabolism of iron (3). Additionally, cells employ proteins of the ferritin-like superfamily to store excess iron as an inert iron mineral phase and thus prevent Fenton chemistry (2). Ferritin-like proteins with iron storage capability are found in the ferritin (Ftn), heme-containing bacterioferritin (Bfr), archaeoferritin (Afr), and DNA-binding proteins from starved cells (Dps) or Dps-like subfamilies (4–6). All of these proteins share a four-helical bundle structural motif and are able to self-assemble into sphere-shaped hollow tetraicosameric (Ftn, Bfr, and Afr) or dodecameric (Dps and Dps-like) nanocages that engulf an iron mineral core (4). Iron mineralization in the interior of the nanocages is catalyzed by a ferroxidase center (FC) which is formed by dinuclear metal ion binding sites in the center of each Ftn and Bfr subunit or at subunit interphases in Dps proteins (7, 8). Most iron-storing ferritin-like proteins form homooligomeric shells and thus have a fixed number of FCs per nanocage. Vertebrate ferritins, however, are heterooligomeric assemblies. In humans, for example, ferritin is composed of heavy (H)- and light (L)-chain ferritins which share only 55% sequence similarity and have different functionalities (9). While H-ferritin provides the FC residues, L-ferritin is thought to enhance oligomer stability and iron influx into the nanocage (10).

A rather unusual role of ferritin-like proteins was proposed for magnetotactic bacteria (MTB) (11). In *Magnetospirillum* species, a ferritin-like component was found to play a major role in the intracellular biomineralization pathway of membrane-enclosed ferrimagnetic magnetite [$\text{Fe}^{2+}(\text{Fe}^{3+})_2\text{O}_4$] crystals, called magnetosomes, which enable magnetospirilla and other MTB to orient themselves along the Earth's magnetic field lines to find growth-favoring anoxic or microoxic zones within their aquatic habitats. Early Mössbauer spectroscopic and electron microscopic analyses indicated that crystallization of magnetite in *Magnetospirillum magnetotacticum* proceeds via precursors, including a ferritin-like ferrihydrite component (12). Using X-ray absorption near-edge structure (XANES) and high-resolution transmission electron microscopy (TEM), Fdez-Gubieda et al. (13) reported that magnetite is also rapidly biomineralized from a ferritin-like ferrihydrite precursor in *Magnetospirillum gryphiswaldense* MSR-1. An investigation on *M. magneticum* revealed the presence of a highly disordered and phosphate-rich ferric hydroxide phase consistent with prokaryotic ferritins outside the magnetosome vesicle (14). Interestingly, in this study the authors could show that this iron mineral phase transforms via purely inorganic ferrihydrite-like nanometric ferric(oxyhydr)oxides to magnetite within the magnetosomes (14). Based on Mössbauer spectroscopic analyses of MSR-1, however, a magnetite biomineralization model without mineral precursor phases was suggested (15). Nevertheless, it was proposed that a ferritin-like compound is required for the release of iron at the magnetosome-compartment interface (15). Preliminary biochemical analyses provided evidence that the ferritin-like ferrihydrite metabolite is of proteinaceous and not inorganic origin (15). The authors could enrich a reddish, high-molecular-mass protein ($M > 100$ kDa) that carried large amounts of iron. However, the ferritin-like component has not been identified at the molecular level yet.

In order to identify the ferritin-like iron metabolite and clarify its role for magnetite biomineralization, we started to analyze ferritin-like proteins of MSR-1. Using genetic, biochemical, and spectroscopic techniques, we show that, contrary to previous assumptions, ferritin-like proteins are not required for magnetite biomineralization but involved in the resistance to oxidative stress. We also provide evidence that Bfr of MSR-1 is a heterotetraicosameric protein complex consisting of subunits with distinct biochemical and catalytic properties. Furthermore, we show that the Bfr1 subunit requires interaction with Bfr2 to form stable nanocages.

RESULTS

Eleven genes encoding proteins with at least partial homology to eight different ferritin-like subfamilies were identified in the genome of MSR-1 (16). However, only three proteins (MSR1_27050 [Bfr1], MSR1_27040 [Bfr2] [bacterioferritins], and MSR1_39700 [Dps]) belonged to subfamilies with the capability to store iron (see Fig. S1A in the supplemental material). Among these, Bfr1 and Bfr2 first caught our attention since both proteins are encoded by genes that are separated by only 11 nt and seem to form a bicistronic operon (Fig. S1B). Furthermore, sequence analyses revealed the lack of a Met residue at position 52 in Bfr1 which is essential for axial heme binding at subunit interfaces (17). Thus, Bfr1 is likely unable to contribute to heme binding. In contrast, several residues of the FC are mutated in Bfr2 (Fig. S1C). These findings suggested that the Bfr proteins of MSR-1 are functionally divergent and might form a heterooligomeric bacterioferritin complex. To test if Bfr1 and Bfr2 indeed interact, a bacterial two-hybrid assay was performed. Therefore, *bfr1* and *bfr2* were cloned in frame with either the N-terminal T25 domain or the C-terminal T18 domain of the *Bordetella pertussis* CyaA adenylate cyclase, respectively. The resulting T18 and T25 plasmids were cotransformed into *Escherichia coli* BTH101 in different combinations with empty pUT18c and pKNT25 vectors as controls. Protein-protein interactions were evaluated after growth of spotted cell suspensions on LB–X-Gal–IPTG plates. While all control strain colonies remained white, strains coexpressing T18-*bfr1* and *bfr1*-T25 or T18-*bfr2* and *bfr2*-T25 formed dark blue colonies, indicating strong self-interactions (Fig. 1A). Interestingly, we also observed a strong interaction in strains coexpressing T18-*bfr1* and *bfr2*-T25, indicating a Bfr heterooligomerization. In contrast, strains coexpressing T18-*bfr2* and *bfr1*-T25 revealed no interaction, which, however, might have been caused by sterical hindrance of the T-domains in a heterooligomeric Bfr complex. To confirm the formation of heterooligomeric nanocages *in vivo*, we next aimed to purify the native protein complex from MSR-1. Unfortunately, various attempts employing classical (heat treatment, butanol extraction, and anion-exchange and size exclusion chromatography [AEC and SEC, respectively]) or recombinant (affinity purification of tagged Bfr) methods were not successful due to the low abundance of the protein, its temperature sensitivity, or its strong tendency to aggregate. Hence, we coexpressed *bfr1* and *bfr2* in *E. coli*. After purification of Bfr by SEC and AEC, four bands were observed on SDS-PAGE: two intense bands at approximately 15 kDa and 18 kDa and two faint bands of 12 and 36 kDa, respectively (Fig. 1B). The small 12-kDa band was attributed to a degradation product because its concentration increased concomitantly to the length of the expression period and was recognized by an anti-Bfr1 antibody. Edman sequencing of the 15-kDa band revealed sequences perfectly matching the N terminus of Bfr1, whereas the sequence from the 18-kDa band was identical to the first 10 aa of Bfr2. For the band at 36 kDa, a 20-aa-long sequence that had 100% identity to Bfr2 could be determined. In contrast to the band at 18 kDa, the 36-kDa band was also stained in immunoblots with anti-Bfr1 antibodies (Fig. 1B), further indicating formation of a heterooligomeric Bfr. However, the presence of two different homooligomers of the same molecular weight (MW) could still not be excluded using SEC and AEC. Therefore, we changed our strategy and used Strep tag affinity purification to isolate Strep-tagged Bfr1. By this method, Bfr2 could be copurified and was present at a similar ratio as Bfr1 as observed with SEC/AEC-purified untagged Bfr (Fig. 1C). Subsequent purification of His-tagged Bfr2 using Ni-NTA affinity chromatography resulted in the removal of the ~12-kDa degradation product, whereas Bfr1 and Bfr2 were still present at similar ratios, indicating that the two proteins were present in the same complex (Fig. 1C). Next, purified Bfr extracts were loaded onto a blue native (BN)-PAGE gel to determine the MW of the complex. This analysis revealed the presence of two distinct bands of ~500 kDa and ~740 kDa, respectively (Fig. 1D). While these results suggested the presence of two different Bfr complexes, 2D-BN/SDS-PAGE analyses revealed that Bfr1 and Bfr2 were present in both high-MW bands (Fig. 1E). Since it is well known that vertebrate ferritins can form dimers (18) and horse spleen ferritin was also separated

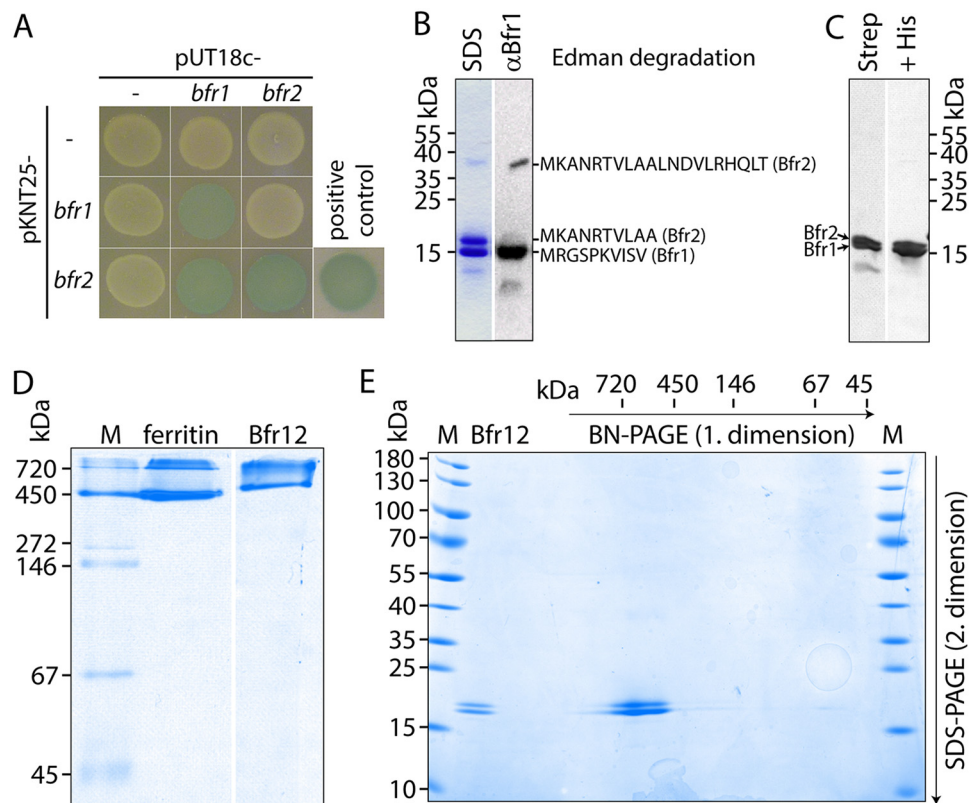


FIG 1 Bfr of MSR-1 is a heterotetraicosamer. (A) Detection of Bfr protein (self-)interactions via bacterial two-hybrid analysis. Five-microliter cell suspensions of *E. coli* BTH101 coexpressing T18 and T25 fusions of *bfr1* and *bfr2* as well as control strains with empty vectors were grown on LB-X-Gal-IPTG medium at 30°C for 20 h. Positive control, *E. coli* BTH101 cotransformed with pKT25-*zip* and pUT18c-*zip*. (B) Coomassie blue-stained SDS-PAGE (13 to 20%) and anti-Bfr1 Western immunoblot analysis of 4 μ g SEC- and AEC-purified, untagged MSR-1 Bfr after overexpression from pET-15b-Bfr in *E. coli* BL21-gold. Sequences retrieved from Edman degradation of the corresponding bands are indicated. (C) Coomassie blue-stained SDS-PAGE (15%) analysis of 4 μ g Strep-tag affinity (left) and Strep-tag plus Ni-NTA-affinity (right)-purified MSR-1 Bfr after overexpression from pET-51b-Bfr12 in *E. coli* Rosetta(DE3)pLys. (D) Coomassie blue-stained 4 to 12% BN-PAGE gel of 6 μ g horse spleen ferritin and 8 μ g tandem-affinity-purified MSR-1 Bfr. M, marker (native marker liquid mix for BN/CN [Serva]). (E) Coomassie blue-stained 2D-BN/SDS-PAGE gel of Strep-tag affinity-purified MSR-1 Bfr after overexpression from pET-51b-Bfr12 in *E. coli* Rosetta(DE3)pLys. The arrow indicates the position and direction of the Bfr-containing BN-PAGE gel slice from the first dimension. Bfr12, 1 μ g of SDS-treated MSR-1 Bfr loaded directly on the SDS-PAGE gel (without previous BN-PAGE). M, marker (prestained PageRuler protein ladder [Thermo Scientific]).

into a 450-kDa monomeric nanocage band and a 720-kDa dimeric nanocage band (Fig. 1D), we assume that the 740-kDa band of MSR-1 Bfr also reflects a dimeric Bfr nanocage fraction. Subsequently, we used transmission electron microscopy (TEM) to estimate the number of subunits of a single Bfr nanocage. The analysis of negatively stained protein complexes revealed an average outer diameter of 11.87 ± 1.02 nm (Fig. S2). Almost-identical complex sizes of 11.95 ± 0.76 nm were observed with tetraicosameric horse spleen ferritin, which suggested that also Bfr of MSR-1 is composed of 24 subunits.

Next, we were interested in the role of iron-storing ferritins for magnetite biomineralization and generated unmarked deletion mutants of *dps* and the *bfr12* operon. TEM analyses showed that both mutants formed magnetite crystals with an average diameter of 33 ± 9.7 nm ($\Delta bfr12$) or 32.4 ± 8.3 nm (Δdps) that were essentially identical to the WT (34.8 ± 10.2 nm). Also, the average numbers of magnetosomes ($\Delta bfr12 = 33.1 \pm 8.5$ cell⁻¹; $\Delta dps = 34.1 \pm 11.1$ cell⁻¹) were similar to the WT 34.3 ± 8.4 cell⁻¹ (Fig. S3), indicating that in both mutants magnetosome formation was not affected. To exclude the possibility that Dps and Bfr complement each other in terms of magnetite biomineralization, we aimed to delete *bfr12* in the *dps* mutant

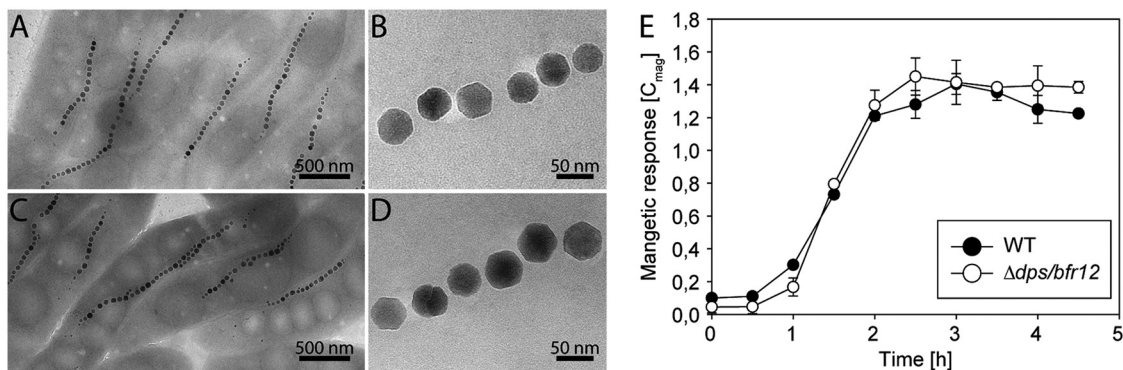


FIG 2 Bfr and Dps are not required for magnetosome formation in MSR-1. (A to D) Representative TEM micrographs of cells and magnetosome particles from MSR-1 WT (A and B) and $\Delta dps/bfr12$ (C and D) after growth under anaerobic conditions. (E) Time course of increase in magnetic response of WT and $\Delta dps/bfr12$ cultures after induction of magnetite biomineralization by addition of 50 μ M iron citrate. Cells were passaged in the absence of iron three times before induction. The assay was performed in triplicate, and values are expressed as means, with standard deviations displayed as error bars.

background. Under microaerobic conditions (2% O_2), only a few clones that still contained the *bfr* genes were obtained. However, under strictly anoxic conditions we succeeded in the generation of the *dps/bfr12* double deletion mutant, suggesting that growth of the *dps/bfr12* mutant might be inhibited by oxygen. Thus, we analyzed magnetosome formation of the *dps/bfr12* mutant after growth under anoxic conditions. Unexpectedly, we failed to detect any significant difference from the WT with respect to magnetic response (WT = 1.42 ± 0.01 versus $\Delta dps/bfr12 = 1.4 \pm 0.03$), magnetosome numbers (WT = 28.2 ± 8.0 cell $^{-1}$ versus $\Delta dps/bfr12 = 28.8 \pm 8.1$ cell $^{-1}$) as well as magnetite crystal diameters (WT = 41.0 ± 11.4 nm versus $\Delta dps/bfr12 = 39.6 \pm 12.0$ nm) or crystal shape (Fig. 2A to D). Also, magnetosome induction experiments by addition of iron to cells grown under iron-limiting conditions revealed no differences between the WT and $\Delta dps/bfr12$ strains. In both strains, the magnetic response started to increase already 30 min after iron induction (Fig. 2E) and reached saturation 2 h postinduction, indicating that the ferritin-like proteins Dps and Bfr are not required for magnetite formation in MSR-1.

Previous studies suggested that a bacterioferritin-like protein corresponds to the conspicuous ferritin-like iron metabolite implicated in magnetosome formation (12–15). To test this assumption, the WT and $\Delta bfr12$ strains were grown in the presence of 40 μ M $^{57}\text{Fe}(\text{citrate})_2$, harvested in late logarithmic growth phase, and subjected to whole-cell transmission Mössbauer spectroscopic (TMS) analysis at 130 K (above the Verwey temperature of magnetite [$T_v = 113$ K]). In spectra of the WT, three iron metabolites could be detected based on their Mössbauer parameters (isomer shift [δ], quadrupole splitting [ΔE_Q], and hyperfine field [Bhf]) (Table 1, subspectra 1 to 4). The major component exhibits two magnetically split sextets typical of magnetite sites A and B (Fig. 3, s2 and s3, respectively). The second component was attributed to a ferrihydrite-like ferric high-spin species (s4) which is a marker for ferritin-like species. Evidence for this classification follows from a comparison of Mössbauer spectra from MSR-1 WT and the magnetite-free $\Delta mamM$ mutant measured at 130 and 4.2 K (19) (Table 1, s8 to s11). A minor doublet in the WT spectrum was attributed to a ferrous high-spin iron [$\text{Fe}^{2+}\text{O}_6(\text{X}_6)^{7-10}$] metabolite (Fig. 3, s1). In $\Delta bfr12$ cells, again, magnetite was identified as the main iron metabolite (Fig. 3, s6 and s7). In addition, a minor doublet component (Fig. 3, s5) belongs to a [$\text{Fe}_4\text{-S}_4$] $^{2+}$ protein (19, 20), which is masked or not present in the WT. However, no ferrihydrite-like component (i.e., ferric high-spin species) was traceable in TMS spectra of the $\Delta bfr12$ mutant. These Mössbauer experiments substantiate that the ferrihydrite signal is caused by the iron mineral core of Bfr and that biosynthesis of magnetite does not require Bfr.

Since the *dps/bfr12* double deletion mutant could be generated only under anaerobic conditions, we suggested that Bfr might be involved in the resistance to oxidative

TABLE 1 Analysis of Mössbauer spectra^a

Sample (whole cells) and subspectrum	Temp (K)	Metabolite	δ (mm s ⁻¹)	ΔE_Q (mm s ⁻¹)	Γ (mm s ⁻¹)	Bhf (T)	Relative area (%)
WT							
1 ^c	130	[Fe ²⁺ O ₆ (X ₆) ⁿ] ⁿ⁻¹⁰	1.26	2.82	0.43		6.1
2	130	Magnetite A	0.38	0	0.3	49.5	23.7
3	130	Magnetite B	0.76	0	0.52	47.5	47.5
4	130	Ferritin-like	0.48	0.75	0.52		22.7
<i>Δbfr12</i>							
5	130	[Fe ₄ -S ₄] ²⁺	0.40	1.04	0.50		3.0
6	130	Magnetite A	0.36	0	0.34	49.3	32.3
7	130	Magnetite B	0.76	0	0.55	47.4	64.7
WT ^d							
8	130	Ferritin-like	0.45	0.67	0.44		30.36
9	4.2	Ferritin-like	0.49	0.00	0.55 ^b	49.5	26.5
<i>ΔmamM</i> ^d							
10	77	Ferritin-like	0.45	0.75	0.45		61.0
11	4.2	Ferritin-like	0.48	0.00	0.58 ^b	47.83	61.8

^aSummary of parameters used to fit the spectra of Fig. 3 and of spectra not shown in this contribution.

^bLine with largest full width at half maximum.

^cA ferrous iron metabolite with similar Mössbauer characteristics has been observed in many bacterial and fungal systems and was identified as cytoplasmic oligomeric ferrous sugar phosphate in *E. coli* (39).

^dData taken from reference 40: spectra document superparamagnetic transitions between 77 and 4.2 K, yielding complete magnetically split species indicating iron mineral cores as in mammalian ferritins.

stress. To confirm this assumption, we tested MSR-1 WT, *Δdps*, *Δbfr12*, *Δdps/bfr12*, and corresponding transcomplemented mutant strains for susceptibility to oxidative stress (Fig. 4A and B). Under oxic conditions (21% O₂), the mutant *Δdps* (+3.6 ± 0.6 h; two-tailed *t* test, *P* value = 0.0039), *Δbfr12* (+3.3 ± 0.7 h, *P* value = 0.0054), and *Δdps/bfr12* (+6.0 ± 0.8 h, *P* value = 0.0002) strains showed significantly prolonged lag phases compared to the WT (20.9 ± 0.3 h). Transcomplementation of the mutant strains with *dps* or *bfr12* partially restored the growth delay. However, lag phases of the *Δbfr12+bfr1* and *Δbfr12+bfr2* transcomplementation strains were almost similar to that of the noncomplemented *Δbfr12* mutant. In the presence of O₂ and H₂O₂, the duration of the lag phase of the WT increased to 24.7 ± 0.6 h. Whereas the lag phase duration of the *Δbfr12* mutant was also moderately increased, strains with a *dps* deletion showed strikingly prolonged lag phases relative to the WT (*Δdps* = +16.9 ± 3.5 h; *Δdps/bfr12* = +30.8 ± 0.9 h). Transcomplementation of *Δdps* and *Δdps/bfr12* strains with *dps* restored lag-phase duration to WT or *Δbfr12* levels, respectively. In contrast, transcomplementation of the *Δdps/bfr12* mutant with *bfr12* had a much weaker effect and reduced the lag phase by only 8 h to +22.8 ± 1.3 h relative to the WT. While these results confirmed our suggestion that Bfr is involved in the resistance to oxidative stress, it remained unclear why the Bfr1 subunit, containing the FC but lacking heme binding residues, was not able to complement the *bfr12* mutant. Previous studies showed that the catalytic activity of Bfr does not depend on heme but requires the FC (17, 21). To analyze Bfr1 in more detail, we overexpressed single *bfr* genes and *bfr12* in *E. coli*. After cell harvest, we already noted differences in the color of the cell pellets of the expression strains: while cell pellets of strains expressing *bfr2* or *bfr12* had a slightly reddish color, *bfr1* expression strains formed beige cell pellets (Fig. S4). We speculated that this difference is related to the heme-binding capability of the expressed subunit(s). Thus, after affinity purification we employed a pyridine hemochrome assay to determine the heme content of Bfr and the single subunits (Fig. 5A and B). Difference spectra of reduced and oxidized Bfr12 yielded a peak at 557 nm which indicated the presence of heme *b* (22), if also in very small amounts (0.24 to 0.6 heme *b* molecules per tetraeicosamer). Slightly lower heme contents were observed with Bfr2 (~0.12 molecules per tetraeicosamer), while no heme could be detected in Bfr1 samples, confirming our initial assumption that Bfr1 is unable to bind

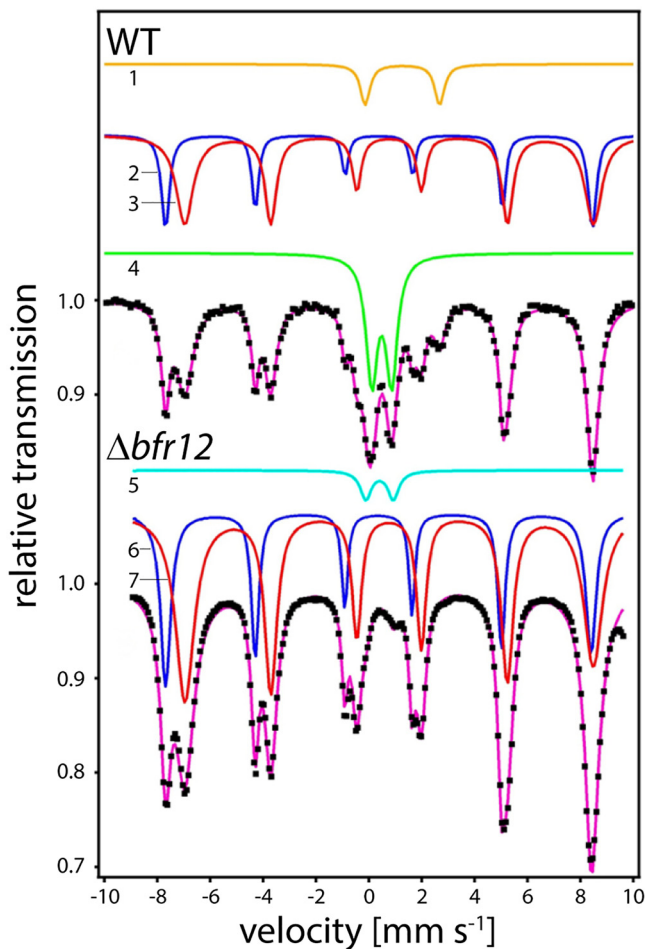


FIG 3 Mössbauer analysis of MSR-1 WT (upper part) and $\Delta bfr12$ (lower part) whole cells. Transmission spectra (purple lines with black dots) were recorded at 130 K. Fitted subspectra of different metabolites are indicated by numbers (1 to 7). Similar metabolites are indicated by similar colors (yellow, blue, turquoise, red, and green, respectively). For details and parameters used to fit metabolite spectra, see Table 1.

heme. Next, the catalytic activities of the bacterioferritins were determined. The heterooligomeric Bfr12 showed the highest activity, whereas both single Bfr subunits revealed iron oxidation rates that were only slightly above the autoxidation control (Fig. 5C). While the low catalytic activities of Bfr1 or Bfr2 explain why they were unable to restore the lag-phase duration of the $\Delta bfr12$ mutant under aerobic conditions, it remained unclear why Bfr1 had such low activities. We thus subjected the single subunits and Bfr12 to BN-PAGE to analyze their oligomeric states. These experiments revealed that Bfr12 (500 and 740 kDa) and Bfr2 (550 kDa) mainly formed high-MW oligomers whereas in the Bfr1 sample only a minor fraction of higher oligomers (500 kDa) and a large fraction of ~ 58 kDa (corresponding to trimers) was observed (Fig. 5D). Consistent with these observations, Bfr2 homooligomeric nanocages with a diameter of 12.16 ± 0.76 nm could be readily observed by TEM while Bfr1 samples contained no or only few nanocage-like structures with a diameter of 13.09 ± 0.84 nm (Fig. 5E). These results indicate that Bfr1, in the absence of Bfr2, fails to efficiently assemble into a functional Bfr complex and explains why expression of *bfr1* alone was unable to complement the $\Delta bfr12$ mutant. To finally prove that Bfr1 and Bfr2 have distinct functions and that the catalytic activity of Bfr12 is based on the FC of Bfr1, we analyzed the ferroxidase activity of a Bfr12 version in which the FC mutations of Bfr2 were introduced into Bfr1 (E18Q, H54A, and H131M). As expected, FC-negative Bfr12

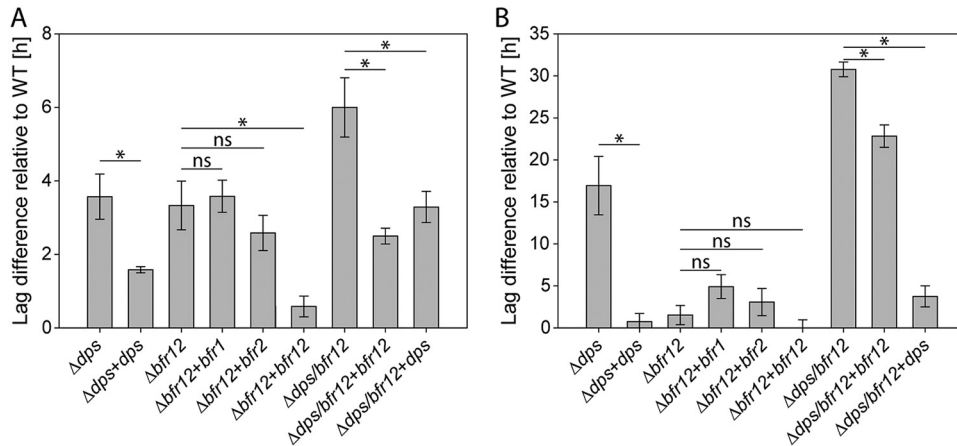


FIG 4 Bfr and Dps protect MSR-1 from oxidative stress. (A) Growth inhibition of MSR-1 strains by oxic conditions (21% O₂). (B) Growth inhibition of MSR-1 strains by oxic conditions (21% O₂) in the presence of H₂O₂. Growth inhibition is expressed as lag-phase duration difference of ferritin-like mutants and transcomplementation strains relative to the WT. Lag-phase duration difference was calculated by measuring the time to grow to an OD₅₆₅ of 0.1 for each strain and subtracting the time that the WT required to grow to the same OD₅₆₅. Values are given as means from at least 4 independent replicates ± standard error of the mean. *, P < 0.05 in two-tailed t test; ns, no significant difference (P ≥ 0.05 in two-tailed t test).

showed drastically reduced iron oxidation rates compared to WT Bfr12 and heme-free Bfr12(M52L) (Fig. 5E and F).

DISCUSSION

In this study, we identified and characterized ferritin-like proteins from MSR-1 to analyze their role during magnetite biomineralization. In contrast to previous reports, which proposed a central role for a ferritin-like component in the magnetite biomineralization pathway (12–15), we were unable to detect any defects or alterations during magnetite biomineralization in the Δdps, Δbfr12, and Δdps/bfr12 ferritin-like mutants. Thus, neither bacterioferritin nor Dps are required for magnetite formation in MSR-1. While it might be possible that other, so-far-uncharacterized, ferritin-like proteins encoded in the genome of MSR-1 are required for magnetite biomineralization, our data indicate that Bfr is identical to the ferritin-like component identified in earlier studies, since ferritin-like signals were absent from the Δbfr12 strain. Therefore, we propose that magnetite biomineralization in MSR-1 is independent of ferritin-like proteins. Furthermore, our results suggest that previous studies, which implicated ferritin-like ferrihydrite in the magnetite biomineralization pathway, simply failed to spatially resolve the independent biomineralization reactions within bacterioferritin and magnetosomes.

Unlike most bacteria with characterized bacterioferritins, MSR-1 contains two distinct bfr genes (bfr1 and bfr2) organized in a putative bicistronic operon. Similar organizations have so far been found only in *Neisseria gonorrhoeae* (23) and *M. magnetotacticum* (24), while distinct bfr genes of cyanobacteria (25) and fluorescent pseudomonads (26) are dispersed in their genomes. Although these studies already suggested the existence of heterooligomeric nanocages, direct evidence that isolated Bfr proteins were located within the same protein complex, and did not represent two different homooligomers, was lacking (23–26). In contrast, using SDS-PAGE analyses of tandem-affinity-purified Bfr, bacterial two-hybrid analysis, and (2D)-BN-PAGE as well as TEM imaging, we could for the first time unequivocally show the formation of a heterooligomeric bacterioferritin consisting of 24 subunits.

Consistent with its phylogenetic affiliation with the Bfr subfamily, heme b was detected in purified Bfr, although at a very low concentration. While similarly low heme contents have been described for Bfr from *E. coli* upon unbalanced overexpression (27), we could show that Bfr1, in contrast to Bfr2, is unable to contribute to heme binding,

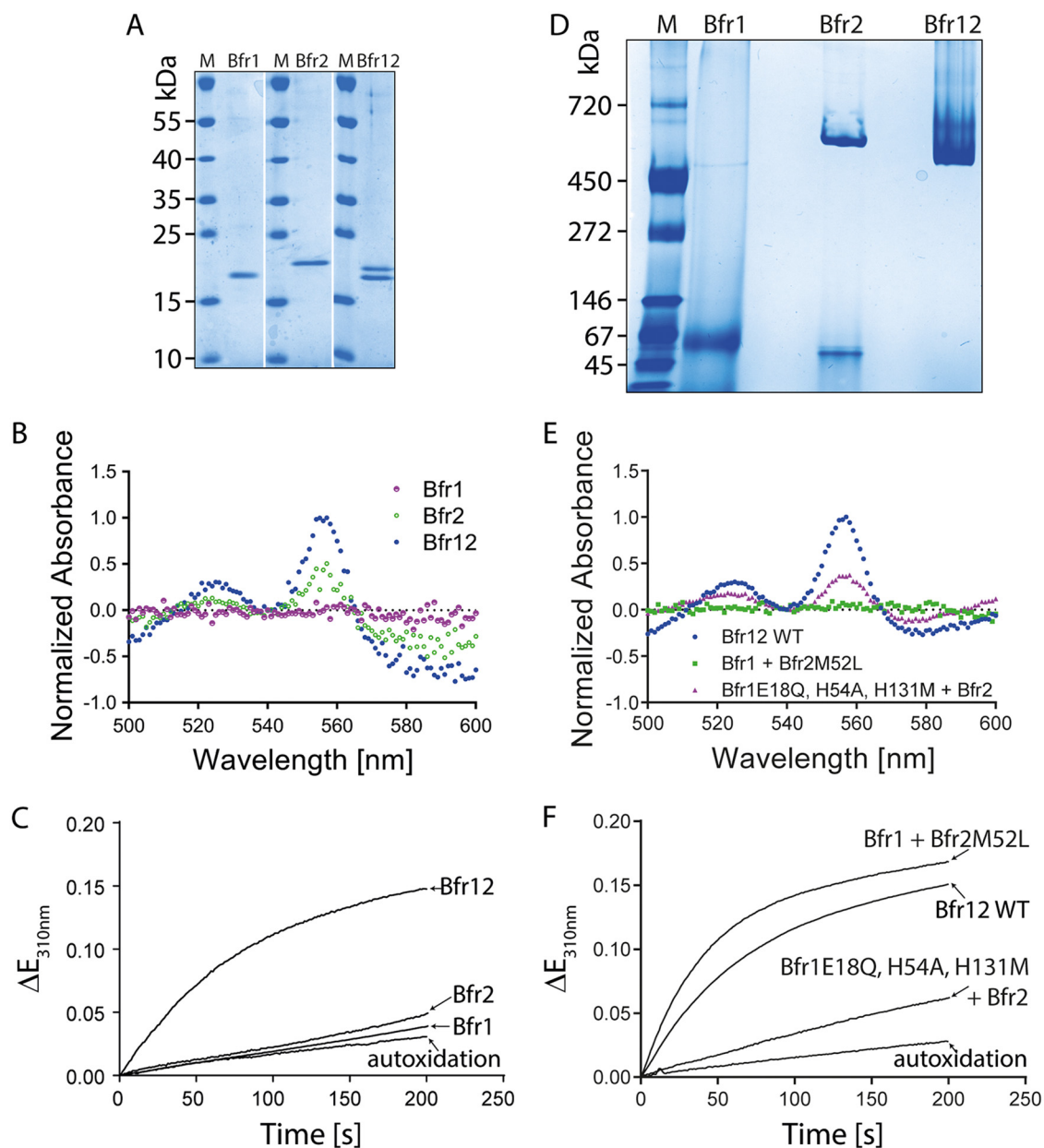


FIG 5 MSR-1 Bfr is composed of functionally distinct subunits. (A) Coomassie blue-stained 8 to 22.5% SDS-PAGE gel with Strep-tag affinity-purified Bfr1 (1 μ g), Bfr2 (1 μ g), and Bfr12 (2 μ g). M, marker (prestained PageRuler protein ladder [Thermo Scientific]). (B) Pyridine hemochrome difference spectra of 50 μ M purified Bfr1, Bfr2, and Bfr12. (C) Absorbance changes measured at 310 nm after the addition of 150 μ M Fe(II)Cl₂ to 1 μ M Bfr1, Bfr2, and Bfr12, respectively. The autoxidation control contained an equal volume of buffer A1 instead of protein solution. (D) Coomassie blue-stained 6 to 15% BN-PAGE gel loaded with 18 μ g Bfr1, 13.5 μ g Bfr2, and 13.5 μ g Bfr12, respectively. M, marker (native marker liquid mix for BN/CN [Serva]). (E) Pyridine hemochrome difference spectra of 50 μ M purified Bfr12, Bfr1 plus Bfr2M52L, and Bfr1E18Q, H54A, H131M plus Bfr2. (F) Absorbance changes measured at 310 nm after the addition of 150 μ M Fe(II)Cl₂ to 1 μ M Bfr12, Bfr1 plus Bfr2M52L, and Bfr1E18Q, H54A, H131M plus Bfr2, respectively. The autoxidation control contained an equal volume of buffer A1 instead of protein solution.

most likely due to the lack of Met52, which is required for axial heme binding between the subunits (17). According to the weaker Bfr2 band intensities relative to those of Bfr1 in SDS-PAGE and 2D-BN-PAGE experiments, we suggest that heterotetraeicosameric nanocages have an unequal Bfr1:Bfr2 subunit stoichiometry of 14:10. Thus, MSR-1 Bfr may contain at maximum five heme *b* binding sites per nanocage, which corresponds to only ~60% of the heme-binding capacity of Bfr from *E. coli* and most likely also contributes to the low heme content of isolated Bfr. Considering the proposed role of heme in facilitating the release of iron from the mineral core (21), and the increased

iron content of heme-free compared to heme-containing Bfr in *E. coli* (17), heterooligomeric Bfrs with only a few heme-binding sites could have evolved to store increased amounts of iron. This might be supported by the fact that heterooligomeric Bfrs have mainly been proposed for organisms with relatively high iron demand (e.g., magnetotactic, photosynthetic, or pathogenic bacteria) (23–25). Furthermore, the reduced number of FCs per oligomer may also contribute to an increased iron storage capability since L-rich ferritins from liver or spleen have been found to incorporate much more iron than H-rich ferritins from heart muscle or brain cells (28).

In contrast to heme binding, residues essential for the ferroxidase activity are conserved in Bfr1 only, since in Bfr2 several ferroxidase site residues are mutated. However, despite the presence of an FC, Bfr1 extracts showed unexpectedly low ferroxidase activities. We suggest that the low catalytic activity of Bfr1 is mainly based on the small amount of Bfr1 homooligomers. This would also be consistent with the finding that expression of *bfr1* alone could not restore the growth of the $\Delta bfr12$ mutant under aerobic conditions. Interestingly, also other organisms, for which a heterooligomeric Bfr has been proposed, seem to require both subunits to assemble functional Bfr complexes. For example, in *Synechocystis* sp. strain PCC 6803, it was observed that upon deletion of *bfrB* (corresponding to Bfr2 from MSR-1), no oligomeric complexes composed of BfrA (corresponding to Bfr1 of MSR-1) could be isolated (25). Similarly, despite the presence of *bfrA*, no iron-containing oligomers could be detected in *N. gonorrhoeae* $\Delta bfrB$ mutants (23). While the structural basis of the poor Bfr1 oligomerization remains to be elucidated, sequence analyses suggest that several exchanges of residues critical for oligomerization of *E. coli* Bfr (K33E, Y45E, D56G, E60N, and E128Q) (29) prevent proper assembly.

With Bfr2, we obtained almost equally low ferroxidase activities as observed with Bfr1. However, in contrast to Bfr1, the majority of Bfr2 was found to be assembled as an oligomer. Thus, the low ferroxidase activity can be directly related to the absence of the FC. This idea is also supported by the low activity of Bfr12 in which the Bfr2 FC mutations were introduced into Bfr1 (E18Q, H54A, and H131M). Thus, the high activity of the heterooligomeric MSR-1 Bfr is mainly caused by the FC of properly assembled Bfr1.

In summary, we showed that in contrast to several previous reports the ferritin-like proteins Bfr and Dps are not involved in magnetite biomineralization. Additionally, we have characterized a heterotetraicosameric bacterioferritin with, similar to vertebrate ferritins, functionally distinct subunits.

MATERIALS AND METHODS

Strains, plasmids, and growth conditions. Bacterial strains and plasmids are described in Text S1 in the supplemental material. *E. coli* strains were grown in lysogeny broth (LB) supplemented with kanamycin (25 $\mu\text{g ml}^{-1}$) or ampicillin (50 $\mu\text{g ml}^{-1}$) at 37°C with vigorous shaking (200 rpm). For cultivation of *E. coli* BW29427, LB was supplemented with DL- α,ϵ -diaminopimelic acid (1 mM). All MSR-1 strains were grown at 28°C or 30°C in modified flask standard medium (FSM) with moderate agitation (120 rpm) under aerobic, microaerobic, or anaerobic conditions (30). To obtain ^{57}Fe -enriched cells for Mössbauer spectroscopic analysis, iron was removed from glassware by three washing steps with 25% (wt/vol) HCl, followed by three rinses with 1/2-volume deionized water. MSR-1 cells were then cultivated in FSM supplemented with 40 μM $^{57}\text{Fe}(\text{citrate})_2$ (31).

Molecular and genetic techniques. Unless specified otherwise, molecular techniques were performed using standard protocols (32). All oligonucleotide primers (Text S1) were purchased from Sigma-Aldrich.

Point mutations were generated using the Phusion site-directed mutagenesis kit (Thermo Scientific).

Generation of MSR-1 mutants. For the generation of unmarked MSR-1 *dps* and *bfr* deletion mutants, ~0.7-kb fragments of the up- and downstream regions of *dps* and *bfr12* were amplified by PCR using Phusion polymerase (New England Biolabs [NEB]) (primers [Text S1]). After gel purification of PCR products, the corresponding up- and downstream fragments were fused by overlap extension PCR with T4 polynucleotide kinase (Thermo Scientific) phosphorylated primers. The fused PCR products were subsequently cloned into dephosphorylated EcoRV-digested pORFM-GalK vector to yield pORFM Δdps and pORFM $\Delta bfr12$, respectively. Deletion vectors were transferred to MSR-1 by conjugation as described previously (33). Kanamycin-resistant plasmid insertion mutants were isolated after incubation for 5 days (30°C, 1.5% O₂), transferred to 100 μl fresh FSM, and grown overnight (30°C, 1.5% O₂). One-hundred-microliter cultures were then inoculated into 900 μl fresh FSM and incubated for 24 h at 30°C and 1.5% O₂ before 100 μl cell culture was plated on FSM agar plates containing 2.5% galactose and 100 ng μl^{-1}

anhydrotetracycline (34). After incubation for 5 days (30°C, 1.5% O₂), mutant colonies were PCR verified and transferred to 100 μl FSM. For deletion of *bfr12* in the Δ *dps* mutant, counterselection on FSM galactose plates was performed by incubation for 14 days under anaerobic conditions at ambient temperature using a Coy anaerobic chamber.

Oxidative stress sensitivity assay. To test growth of MSR-1 in the presence of O₂ and/or H₂O₂, the WT, mutant, and pBam1-transcomplemented mutant strains (Table S1) were passaged three times in 3 ml FSM (without antibiotics) overnight at 28°C with 2% O₂. Cultures were then diluted to an OD₅₆₅ of 0.1 in FSM, and 100 μl of diluted cultures was used to inoculate 900 μl FSM containing 10 μM H₂O₂ (Merck). Aerobic growth (21% O₂) at 141 rpm and 28°C was monitored every 20 min at 565 nm with an Infinite 200pro microplate reader (Tecan) for 80 h.

Cloning, expression, and purification of recombinant MSR-1 Bfr. Bfr from MSR-1 was overexpressed from pET-15b-Bfr in *E. coli* BL21-Gold cells and purified by SEC and AEC. Additionally, Bfr1, Bfr2, and Bfr12 were produced from pET-51b-Bfr1, pET-51b-Bfr2, and pET-51b-Bfr12 in *E. coli* Rosetta(DE3)pLysS, respectively (detailed methods for plasmid construction, gene expression, and protein purification are provided in Text S1).

Determination of Bfr heme content. Heme contents were determined by a pyridine hemochrome assay (35). Reduced minus oxidized difference spectra were recorded to identify heme groups. Heme concentrations were calculated applying a differential extinction coefficient, $\epsilon_{557-540\text{nm}} = 22.1 \text{ M}^{-1} \text{ cm}^{-1}$ (35).

N-terminal Edman sequencing. Purified Bfr12 was electroblotted on a PVDF membrane and stained with freshly prepared 0.1% Coomassie R-250 (in 40% methanol) and 1% acetic acid for 30 s. Destaining was performed with 50% methanol until the background was clear and bands were visible. The membrane was air dried, bands were cut, and N-terminal Bfr subunit amino acid sequences were determined by Edman degradation.

BN-PAGE and 2D-BN/SDS-PAGE analyses. To separate proteins by their native MW, we used 6 to 12% or 6 to 15% polyacrylamide gradient gels for BN-PAGE analyses as described previously (36). Therefore, Bfr12 samples were dialyzed against 50 mM imidazole-HCl, 50 mM NaCl, pH 7, at 4°C overnight (Visking type 8/32; MW cutoff [MWCO], 14 kDa [Carl Roth]). Alternatively, Bfr2 and Bfr1 plus -2 protein samples were adjusted to a concentration of 4.5 mg ml⁻¹ in buffer A1 and diluted by addition of 50 mM Tris-HCl, pH 8.0, and 10× BN-PAGE loading buffer (50% [wt/vol] glycerol, 0.1% [wt/vol] Ponceau S) to a final concentration of 450 μg ml⁻¹ (~22 μM) protein, 5% (wt/vol) glycerol, and 0.01% (wt/vol) Ponceau S in 50 mM Tris-HCl, 50 mM NaCl, pH 8.0. Bfr1 samples were adjusted to a concentration of 6 mg ml⁻¹ in buffer A1 and then diluted to a final concentration of 600 μg ml⁻¹ (~30 μM) protein, 5% (wt/vol) glycerol, and 0.01% (wt/vol) Ponceau S in 50 mM Tris-HCl, 50 mM NaCl, pH 8.0. Of these samples, 30 μl was loaded onto BN-PAGE gels with 10 μl of native marker liquid mix (Serva) as a control. The gels were then run at 4°C, 100 V, and 15 mA. After the run front reached one-third of the total run, the cathode buffer B (7.5 mM imidazole, 50 mM Tricine, 0.02% [wt/vol] Coomassie brilliant blue G-250) was replaced with cathode buffer B/10 (7.5 mM imidazole, 50 mM Tricine, 0.002% [wt/vol] Coomassie brilliant blue G-250), and the run was continued until the run front reached the end of the gel. BN-PAGE gels were then stained with Coomassie brilliant blue R-250 or subjected to 2D-BN/SDS-PAGE analysis.

For 2D-BN/SDS-PAGE, lanes of interest were cut out from BN-PAGE gels, briefly heated in 1% (wt/vol) SDS with 10 mM DTT, and equilibrated for 20 min. Treated gel strips were then clamped between glass plates of a gel casting apparatus, and an 8 to 22.5% gradient separation gel was poured underneath the gel strips. After polymerization, a 5% stacking gel was cast below the gel strip. After 4 μl PageRuler prestained protein ladder (Thermo Scientific) and 1 μg SDS-treated sample of the same protein from the first dimension were loaded, the SDS-PAGE gels were run at 25 mA per gel and 300 V for 3 h at room temperature (RT). Subsequently, gels were stained with Coomassie brilliant blue R-250.

Determination of ferroxidase activities. For the measurement of the ferroxidase activity, 1 μM Bfr was incubated with 150 μM FeCl₂ in a total volume of 200 μl at 27°C, and the absorbance at 310 nm was measured over a period of 200 s (Evolution 201 UV-Vis spectrophotometer; Thermo Scientific). For this purpose, 178 μl of 50 mM MOPS, 50 mM NaCl, pH 7, mixed with 20 μl of 10 μM respective Bfr was used as a reference, and the reaction was started by the addition of 2 μl of 15 mM FeCl₂ solution. As a negative control, 20 μl of buffer A1 was added instead of Bfr.

Transmission Mössbauer spectroscopy. For TMS analyses, MSR-1 WT, Δ *mamM*, and Δ *bfr12* strains were grown in ⁵⁷Fe-enriched medium and harvested at late exponential phase. Cell pellets were weighed, transferred into Delrin Mössbauer sample holders, frozen in liquid nitrogen, and kept at this temperature and in part at -80°C until measurement except for overnight transport on dry ice. The Mössbauer spectra were recorded in the horizontal transmission geometry using a constant acceleration spectrometer operated in conjunction with a 512-channel analyzer in the time scale mode. The detector consisted of a proportional counter filled with argon-methane (9:1). The source was at room temperature and consisted of 0.7 to 0.2 GBq [⁵⁷Co] diffused in Rh foil (WissEl). The spectrometer was calibrated against α -iron at room temperature (RT). For measurements at 130 and 77 K, samples were placed in a continuous-flow cryostat (Oxford Instruments). For measurements at 4.2 K, a helium bath cryostat (MD306; Oxford Instruments) was employed. The ⁵⁷Co source exhibiting an activity of 0.19 GBq was sealed in an Rh matrix at RT and was mounted on a constant-velocity drive. The detector consisted of a proportional counter made in-house and filled with argon-methane (90:10). Spectral data were buffered in a multichannel analyzer and transferred to a PC for further analysis, employing the Vinda program on an Excel 2003 platform (37). Isomer shifts δ , quadrupole splittings ΔE_Q and Bhf, and percentages of the total absorption area were obtained by least-squares fits of Lorentzian lines to the experimental spectra.

Transmission electron microscopy. For TEM analysis, unstained cells were concentrated, adsorbed onto carbon- or Ploioform-coated copper grids, and washed two times with ddH₂O (38). For TEM of Bfr and horse spleen ferritin samples, protein solutions were adsorbed on a carbon-coated copper grid for 10 min. Then, the grid was incubated for 3 min on uranyl acetate (2% [wt/vol]) for negative contrast and washed with ddH₂O once. Bright-field TEM was performed on an FEI Tecnai F20 (FEI) or Zeiss EM902A (Zeiss) transmission electron microscope using an accelerating voltage of 200 kV or 80 kV, respectively. For data processing, interpretation, and analysis, the software packages DigitalMicrograph (Gatan) and ImageJ (NIH) were used. For determinations of magnetite particle numbers per cell, at least 100 cells were analyzed and at least 450 particles were measured for analysis of magnetite particle diameters. For determination of Bfr and ferritin diameters, at least 100 particles were analyzed.

SUPPLEMENTAL MATERIAL

Supplemental material for this article may be found at <https://doi.org/10.1128/mBio.02795-18>.

TEXT S1, DOCX file, 0.01 MB.

FIG S1, TIF file, 2.4 MB.

FIG S2, TIF file, 2.4 MB.

FIG S3, TIF file, 2 MB.

FIG S4, TIF file, 1.5 MB.

TABLE S1, DOCX file, 0.02 MB.

ACKNOWLEDGMENTS

We thank Rainer Bartels for performing automated Edman degradation (Forschungszentrum Borstel, Structural Biochemistry, Germany).

We are indebted to the Deutsche Forschungsgemeinschaft (DFG) for grants Ma 916/21-1 (B.F.M.) and Schu 1080/13-1 (D.S.). This project has received funding from the European Research Council (ERC) under the European Union's Horizon 2020 research and innovation programme (grant agreement 692637).

REFERENCES

- Andrews SC, Robinson AK, Rodríguez-Quiriones F. 2003. Bacterial iron homeostasis. *FEMS Microbiol Rev* 27:215–237. [https://doi.org/10.1016/S0168-6445\(03\)00055-X](https://doi.org/10.1016/S0168-6445(03)00055-X).
- Imlay JA, Linn S. 1988. DNA damage and oxygen radical toxicity. *Science* 240:1302–1309. <https://doi.org/10.1126/science.3287616>.
- Escolar L, Pérez-Martín J, de Lorenzo V. 1999. Opening the iron box: transcriptional metalloregulation by the Fur protein. *J Bacteriol* 181:6223–6229.
- Andrews SC. 2010. The ferritin-like superfamily: evolution of the biological iron storeman from a rubrerythrin-like ancestor. *Biochim Biophys Acta* 1800:691–705. <https://doi.org/10.1016/j.bbagen.2010.05.010>.
- Ebrahimi KH, Hagedoorn P-L, van der Weel L, Verhaert PD, Hagen WR. 2012. A novel mechanism of iron-core formation by *Pyrococcus furiosus* archaeoferritin, a member of an uncharacterized branch of the ferritin-like superfamily. *J Biol Inorg Chem* 17:975–985. <https://doi.org/10.1007/s00775-012-0913-0>.
- Reindel S, Anemüller S, Sawaryn A, Matzanke BF. 2002. The DpsA-homologue of the archaeon *Halobacterium salinarum* is a ferritin. *Biochim Biophys Acta* 1598:140–146. [https://doi.org/10.1016/S0167-4838\(02\)00361-8](https://doi.org/10.1016/S0167-4838(02)00361-8).
- Grant RA, Filman DJ, Finkel SE, Kolter R, Hogle JM. 1998. The crystal structure of Dps, a ferritin homolog that binds and protects DNA. *Nat Struct Mol Biol* 5:294–303. <https://doi.org/10.1038/nsb0498-294>.
- Ren B, Tibbelin G, Kajino T, Asami O, Ladenstein R. 2003. The multi-layered structure of Dps with a novel di-nuclear ferroxidase center. *J Mol Biol* 329:467–477. [https://doi.org/10.1016/S0022-2836\(03\)00466-2](https://doi.org/10.1016/S0022-2836(03)00466-2).
- Andrews SC, Smith JM, Yewdall SJ, Guest JR, Harrison PM. 1991. Bacterioferritins and ferritins are distantly related in evolution. Conservation of ferroxidase-centre residues. *FEBS Lett* 293:164–168. [https://doi.org/10.1016/0014-5793\(91\)81177-A](https://doi.org/10.1016/0014-5793(91)81177-A).
- Santambrogio P, Levi S, Arosio P, Palagi L, Vecchio G, Lawson DM, Yewdall SJ, Artymiuk PJ, Harrison PM, Jappelli R. 1992. Evidence that a salt bridge in the light chain contributes to the physical stability difference between heavy and light human ferritins. *J Biol Chem* 267:14077–14083.
- Uebe R, Schüler D. 2016. Magnetosome biogenesis in magnetotactic bacteria. *Nat Rev Microbiol* 14:621–637. <https://doi.org/10.1038/nrmicro.2016.99>.
- Frankel RB, Papaefthymiou GC, Blakemore RP, O'Brien W. 1983. Fe₃O₄ precipitation in magnetotactic bacteria. *Biochim Biophys Acta* 763:147–159. [https://doi.org/10.1016/0167-4889\(83\)90038-1](https://doi.org/10.1016/0167-4889(83)90038-1).
- Fdez-Gubieda ML, Muela A, Alonso J, García-Prieto A, Olivi L, Fernández-Pacheco R, Barandiarán JM. 2013. Magnetite biomineralization in *Magnetospirillum gryphiswaldense*: time-resolved magnetic and structural studies. *ACS Nano* 7:3297–3305. <https://doi.org/10.1021/nn3059983>.
- Baumgartner J, Morin G, Menguy N, Perez Gonzalez T, Widdrat M, Cosmidis J, Faivre D. 2013. Magnetotactic bacteria form magnetite from a phosphate-rich ferric hydroxide via nanometric ferric (oxyhydr)oxide intermediates. *Proc Natl Acad Sci U S A* 110:14883–14888. <https://doi.org/10.1073/pnas.1307119110>.
- Faivre D, Böttger LH, Matzanke BF, Schüler D. 2007. Intracellular magnetite biomineralization in bacteria proceeds by a distinct pathway involving membrane-bound ferritin and an iron(II) species. *Angew Chem Int Ed* 46:8495–8499. <https://doi.org/10.1002/anie.200700927>.
- Uebe R, Schüler D, Jogler C, Wiegand S. 2018. Reevaluation of the complete genome sequence of *Magnetospirillum gryphiswaldense* MSR-1 with single-molecule real-time sequencing data. *Genome Announc* 6:e00309-18. <https://doi.org/10.1128/genomeA.00309-18>.
- Andrews SC, Brun NEL, Barynin V, Thomson AJ, Moore GR, Guest JR, Harrison PM. 1995. Site-directed replacement of the coaxial heme ligands of bacterioferritin generates heme-free variants. *J Biol Chem* 270:23268–23274. <https://doi.org/10.1074/jbc.270.40.23268>.
- Niitsu Y, Listowsky I. 1973. Mechanisms for the formation of ferritin oligomers. *Biochemistry (Mosc)* 12:4690–4695. <https://doi.org/10.1021/bi00747a023>.
- Uebe R, Junge K, Henn V, Poxleitner G, Katzmann E, Plitzko JM, Zarivach R, Kasama T, Wanner G, Pósfai M, Böttger L, Matzanke B, Schüler D. 2011. The cation diffusion facilitator proteins MamB and MamM of *Magnetospirillum gryphiswaldense* have distinct and complex functions, and are involved in magnetite biomineralization and magnetosome membrane assembly. *Mol Microbiol* 82:818–835. <https://doi.org/10.1111/j.1365-2958.2011.07863.x>.

20. Schünemann V, Winkler H. 2000. Structure and dynamics of biomolecules studied by Mössbauer spectroscopy. *Rep Prog Phys* 63:263–353. <https://doi.org/10.1088/0034-4885/63/3/202>.
21. Yasmin S, Andrews SC, Moore GR, Le Brun NE. 2011. A new role for heme, facilitating release of iron from the bacterioferritin iron biomineral. *J Biol Chem* 286:3473–3483. <https://doi.org/10.1074/jbc.M110.175034>.
22. Falk JE. 1964. Porphyrins and metalloporphyrins: their general, physical and coordination chemistry, and laboratory methods, 2nd ed. Elsevier, Amsterdam, Netherlands.
23. Chen CY, Morse SA. 1999. *Neisseria gonorrhoeae* bacterioferritin: structural heterogeneity, involvement in iron storage and protection against oxidative stress. *Microbiology* (Reading, England) 145: 2967–2975. <https://doi.org/10.1099/00221287-145-10-2967>.
24. Bertani LE, Huang JS, Weir BA, Kirschvink JL. 1997. Evidence for two types of subunits in the bacterioferritin of *Magnetospirillum magnetotacticum*. *Gene* 201:31–36. [https://doi.org/10.1016/S0378-1119\(97\)00424-1](https://doi.org/10.1016/S0378-1119(97)00424-1).
25. Keren N, Aurora R, Pakrasi HB. 2004. Critical roles of bacterioferritins in iron storage and proliferation of cyanobacteria. *Plant Physiol* 135: 1666–1673. <https://doi.org/10.1104/pp.104.042770>.
26. Chen S, Bleam WF, Hickey WJ. 2010. Molecular analysis of two bacterioferritin genes, *bfr α* and *bfr β* , in the model rhizobacterium *Pseudomonas putida* KT2440. *Appl Environ Microbiol* 76:5335–5343. <https://doi.org/10.1128/AEM.00215-10>.
27. Jung Y, Kwak J, Lee Y. 2001. High-level production of heme-containing holoproteins in *Escherichia coli*. *Appl Microbiol Biotechnol* 55:187–191. <https://doi.org/10.1007/s002530000502>.
28. Arosio P, Levi S. 2002. Ferritin, iron homeostasis, and oxidative damage. *Free Radic Biol Med* 33:457–463. [https://doi.org/10.1016/S0891-5849\(02\)00842-0](https://doi.org/10.1016/S0891-5849(02)00842-0).
29. Zhang Y, Raudah S, Teo H, Teo GWS, Fan R, Sun X, Orner BP. 2010. Alanine-shaving mutagenesis to determine key interfacial residues governing the assembly of a nano-cage maxi-ferritin. *J Biol Chem* 285: 12078–12086. <https://doi.org/10.1074/jbc.M109.092445>.
30. Barber-Zucker S, Uebe R, Davidov G, Navon Y, Sherf D, Chill JH, Kass I, Bitton R, Schüler D, Zarivach R. 2016. Disease-homologous mutation in the cation diffusion facilitator protein MamM causes single-domain structural loss and signifies its importance. *Sci Rep* 6:31933. <https://doi.org/10.1038/srep31933>.
31. Uebe R, Voigt B, Schweder T, Albrecht D, Katzmann E, Lang C, Böttger L, Matzanke B, Schüler D. 2010. Deletion of a *fur*-like gene affects iron homeostasis and magnetosome formation in *Magnetospirillum gryphiswaldense*. *J Bacteriol* 192:4192–4204. <https://doi.org/10.1128/JB.00319-10>.
32. Sambrook J, Russell D. 2001. Molecular cloning. A laboratory manual. Cold Spring Harbor Laboratory Press, Cold Spring Harbor, NY.
33. Lohße A, Kolinko I, Raschdorf O, Uebe R, Borg S, Brachmann A, Pitzko JM, Müller R, Zhang Y, Schüler D. 2016. Overproduction of magnetosomes by genomic amplification of biosynthetic gene clusters in a magnetotactic bacterium. *Appl Environ Microbiol* 82:3032–3041. <https://doi.org/10.1128/AEM.03860-15>.
34. Uebe R, Keren-Khadmy N, Zeytuni N, Katzmann E, Navon Y, Davidov G, Bitton R, Pitzko JM, Schüler D, Zarivach R. 2018. The dual role of MamB in magnetosome membrane assembly and magnetite biomineralization. *Mol Microbiol* 107:542–557. <https://doi.org/10.1111/mmi.13899>.
35. Williams JN, Jr. 1964. A method for the simultaneous quantitative estimation of cytochromes a, b, c₁, and c in mitochondria. *Arch Biochem Biophys* 107:537–543. [https://doi.org/10.1016/0003-9861\(64\)90313-3](https://doi.org/10.1016/0003-9861(64)90313-3).
36. Wittig I, Braun H-P, Schägger H. 2006. Blue native PAGE. *Nat Protoc* 1:418–428. <https://doi.org/10.1038/nprot.2006.62>.
37. Gunnlaugsson HP. 2016. Spreadsheet based analysis of Mössbauer spectra. *Hyperfine Interact* 237:79. <https://doi.org/10.1007/s10751-016-1271-z>.
38. Zeytuni N, Uebe R, Maes M, Davidov G, Baram M, Raschdorf O, Friedler A, Miller Y, Schüler D, Zarivach R. 2014. Bacterial magnetosome biomineralization—a novel platform to study molecular mechanisms of human CDF-related type-II diabetes. *PLoS One* 9:e97154. <https://doi.org/10.1371/journal.pone.0097154>.
39. Böhnke R, Matzanke BF. 1995. The mobile ferrous iron pool in *Escherichia coli* is bound to a phosphorylated sugar derivative. *Biometals* 8:223–230.
40. Mørup S. 2011. Magnetic relaxation phenomena, p 201–234. *In* Gülich P, Bill E, Trautwein AX (ed), Mössbauer spectroscopy and transition metal chemistry. Springer, Berlin, Germany.